Supplementary Information

Built-In Electric Fields and Ir-Cl Motifs at Heterointerfaces Enable Selective and Durable Seawater Electrolysis

Yaohai Cai,[1,+] Di Liu,[2,+] Dong Liu,[1,] Haoqiang Ai,[3] Kai Liu,[1] Xiaotian Wei,[1] Yingwei Qi,[1] Hui Pan,[2,4] Lei Wang,[1] and Zhenbo Wang [5,*]*

[1]Guangdong Provincial Key Laboratory of New Energy Materials Service Safety, College of Materials Science and Engineering, Shenzhen University, Shenzhen 518060, China

[2]Institute of Applied Physics and Materials Engineering, University of Macau, Macao SAR 999078, China

[3]Thermal Science Research Center, Shandong Institute of Advanced Technology, Jinan 250103, China

[4]Department of Physics and Chemistry, Faculty of Science and Technology, University of Macau, Macao SAR 999078, China

[5]State Key Laboratory of Space Power-Sources, MIIT Key Laboratory of Critical Materials Technology for New Energy Conversion and Storage, School of Chemistry and Chemical Engineering, Harbin Institute of Technology, Harbin 150001, China

[+] These authors contributed equally to this work

Corresponding authors
Dong Liu, email: dongliu@szu.edu.cn
Zhenbo Wang, email: wangzhb@hit.edu.cn

Supplementary Methods

Materials

Iron foam (IF), nickel-molybdenum foam (NiMo), nickel nitrate ($Ni(NO_3)_2 \cdot 6H_2O$; purity ≥98%), iridium chloride hydrate ($IrCl_3 \cdot xH_2O$; purity ≥98%), potassium hydroxide (KOH; purity ≥98%), and commercial RuO_2. Hydrochloric acid, acetone, absolute alcohol, and deionized water with a resistivity of 18.2 MΩ were utilized in all experiments. Additionally, seawater was sourced from the South China Sea (Shenzhen Bay).

Synthesis of NiFe LDH@IF

The NiFe LDH@IF catalyst was fabricated via a one-step immersion method. First, iron foam (IF, 4 × 3 cm^2) was washed with acetone for 10 min to remove organic contaminants, followed by washing with ethanol for 10 min to remove residual acetone. Subsequently, the sample was treated with 1 M dilute hydrochloric acid for 10 min to remove surface oxides, and finally washed with deionized water for 10 min to remove residual hydrochloric acid before use. To prepare the solution, 5 mmol of nickel nitrate hexahydrate ($Ni(NO_3)_2 \cdot 6H_2O$) was dissolved in 50 mL of deionized water under stirring for 30 minutes. The solution was then transferred to a beaker, and the cleaned IF was immersed in the $Ni(NO_3)_2$ solution at room temperature for 3 hours. Finally, the sample was taken out, rinsed with deionized water, and dried to obtain the NiFe LDH@IF.

Synthesis of Ir@IF

The Ir@IF catalyst was synthesized via a one-step immersion method. First, iron foam (IF, 4 × 3 cm^2) was washed with acetone for 10 min to remove organic contaminants, followed by washing with ethanol for 10 min to remove residual acetone. Subsequently, the sample was treated with 1 M dilute hydrochloric acid for 10 min to remove surface oxides, and finally washed with deionized water for 10 min to remove residual hydrochloric acid before use. For the precursor solution, 0.2 mmol iridium trichloride hydrate ($IrCl_3 \cdot xH_2O$) was dissolved in 40 mL of deionized water under magnetic stirring for 30 minutes. The solution was then transferred to a beaker, and the pre-cleaned IF was immersed in the $IrCl_3$ solution at 90 °C for 1 hour. Finally, the sample was retrieved, thoroughly rinsed with deionized water, dried, and collected as the Ir@IF.

Synthesis of Ir/NiFe LDH@IF

The Ir/NiFe LDH@IF catalyst was synthesized via a two-step immersion method. First, iron foam (IF, 4 × 3 cm^2) was washed with acetone for 10 min to remove organic contaminants, followed by washing with ethanol for 10 min to remove residual acetone. Subsequently, the sample was treated with 1 M dilute hydrochloric acid for 10 min to remove surface oxides, and finally washed with deionized water for 10 min to remove residual hydrochloric acid before use. For the first step, 0.2 mmol iridium trichloride hydrate ($IrCl_3 \cdot xH_2O$) was dissolved in 40 mL of deionized water under magnetic stirring for 30 minutes. The solution was transferred to a beaker, and the pre-cleaned IF

was immersed in the $IrCl_3$ solution at 90 °C for 1 hour. The resulting sample was retrieved, thoroughly rinsed with deionized water, and dried to obtain the Ir@IF precursor.
For the second step, 5 mmol nickel nitrate hexahydrate ($Ni(NO_3)_2 \cdot 6H_2O$) was dissolved in 50 mL of deionized water under stirring for 30 minutes. The solution was then transferred to a beaker, and the Ir@IF precursor was immersed in the ($Ni(NO_3)_2$ solution at room temperature for 3 hours. Finally, the product was collected, rinsed with deionized water, dried, and denoted as Ir/NiFe LDH@IF.

Synthesis of RuO_2 catalysts on Iron foam

The 20 mg of RuO_2, 60 μL Nafion, 540 μL deionized water, and 400 μL anhydrous ethanol was mixed. The above mixed slurry was ultrasonically treated for 30 minutes. The 200 μL solution dropwise to 1.5 × 1 cm^2 IF, and then the IF was placed under a baking lamp for 15 minutes.

Materials characterization

The morphologies and dimensions of the catalysts were measured using Scanning electron microscopy (SEM) analyses (Hitachi S-8200). Transmission electron microscopy (TEM) and high-resolution transmission electron microscopy (HR-TEM) images were captured with a JEM2100UHR instrument. Crystal structures were determined by powder X-ray diffraction (X'Pert PRO MPD system) operating at 40 kV and 30 mA with Cu Kα radiation (λ = 1.5418 Å). X-ray photoelectron spectroscopy (XPS) assessments were carried out using an AXIS SUPRA equipped with a monochromatic Al Kα source at 15 mA and 14 kV. XPS spectra were calibrated against the carbon 1s peak, setting the main line to 284.8 eV. DEMS measurements were carried out using a Linglu Instruments QAS 100 device. The X-ray absorption fine structure (XAFS) was obtained by the Taiwan photon source 44A beamline quick scanning X-ray absorption spectrum (Hsinchu). The Ni K-edge, Mn K-edge and Ir l_3-edge XAFS spectra were collected at room temperature and analyzed using Athena and Artemis programs. In-situ Raman spectra were collected with an Invia Qontor Raman spectroscopy system utilizing a 532 nm laser. Electrochemical in situ ATR-FTIR spectra of the samples during electrocatalysis were collected using an external reflection electrochemical cell mounted on a Pike Veemax I ATR accessory in external reflection mode with a silicon crystal. The spectral data were recorded using a Thermo Nicolet Nexus 670 spectrometer. Zeta potential was measured on the Anton Paar surpass 3 and the pH of the solution was 12. UV-vis diffuse reflectance spectra (DRS) were recorded using the SHIMADZU UV-3600iPlus spectrophotometer. Ultraviolet photoemission spectroscopy (UPS) was performed using the Thermo Fisher Scientific Nexsa analyzer using a monochromatic He I light source at a bias of 10 eV. The work function for Au was used as thestandard sample, and the work function Φ was calculated using the following formula:

$$\Phi = h\nu - (E_C - E_F)$$

where the photon energy is 21.2 eV, and E_C and E_F are the inelastic electron cutoff energy and Fermi level, respectively.

Electrochemical measurements

Electrochemical evaluations of all samples were performed using CHI660E, CHI760E, DH7006A-2, and DH7006B-2 stations in an alkaline seawater electrolyte, prepared by adding 1 M KOH to natural, unpurified seawater collected from the South China Sea. A Hg/HgO electrode and a graphite rod served as the reference and counter electrodes, respectively, for the oxygen evolution reaction (OER) and hydrogen evolution reaction (HER). All the prepared samples were utilized as working electrodes. Potentials in these experiments were adjusted to the reversible hydrogen electrode (RHE) standard using the formula: E_{RHE}= E + 0.098 V + 0.059 × pH. The electrocatalytic performance was assessed in various electrolytes: 1.0 M KOH and 1.0 M KOH seawater solution. Linear sweep voltammetry (LSV) with a scan rate of 5 mV s^{-1} was employed to evaluate the OER and HER activities. Tafel slopes were determined from the linear regions of the Tafel plots using the Tafel equation upon LSV curves with iR compensation. Cyclic voltammetry (CV) tests were performed at varying scan rates (20, 40, 60, 80, and 100 mV s^{-1}) to determine the double-layer capacitance (C_{dl}) of the catalysts. For corrosion analysis, the electrochemically active surface area (ECSA) was estimated according to ECSA = C_{dl} / C_s using a specific capacitance (C_s) of 0.040 mF cm^{-2}, and the corrosion current was normalized to ECSA to obtain the corresponding corrosion current density. Electrochemical impedance spectroscopy (EIS) was conducted across a frequency range of 0.01 kHz to 10000 kHz. Long-term stability was assessed via chronopotentiometry at room temperature. The synthesized sample, Ag/AgCl electrode and Pt wire were used as working electrode, reference electrode and counter electrode, respectively. The measurement was carried out in 1 M potassium hydroxide with a potential range from 0.1 V to 0.6 V (vs. Ag/AgCl). After 15 s of testing, data were collected.

DFT calculation

Our first-principles calculations were carried out using the Vienna Ab initio Simulation Package within the framework of density functional theory (DFT)[1,2]. The projector augmented wave pseudo-potentials method[3] and Perdew–Burke–Ernzerhof (PBE) functional[4] under the generalized gradient approximation were applied. To describe localized d-electron interactions, PBE + U calculations was utilized with effective Hubbard U values of 4.3 eV and 5.5 eV for Fe and Ni, respectively[5]. Models of Ir (111), and NiFe LDH (012) slabs were used to construct the heterostructure. A vacuum region of 15 Å along the vertical direction was set to avoid interaction between repeating slabs. Plane-wave cutoff energy was set to 400 eV, with convergence thresholds of 10^{-5} eV for energy and 0.03 eV/Å for force. Van der Waals corrections were applied via the DFT-D3 method[6]. The 2×2×1 and 3×3×1 Monkhorst-Pack[7] type *k*-point sampling were used for structure optimization and surface calculations, respectively. The top two layers and adsorbates were relaxed during optimization, with other layers fixed. Bader's approach[8] was used to calculate the charge transfer between the Ir and NiFe LDH. The atomic structures were visualized using the Atomic Simulation Environment (ASE)[9].

The computational standard hydrogen electrode (SHE) model proposed by Nørskov et

al[10] was employed to evaluate the free energy change of each elementary step of OER. According to this model, the proton-electron pair's free energy equals half the chemical potential of H_2 gas under SHE conditions[11]. For the chlorine evolution reaction (CER), equilibrium between Cl^-(aq) and 1/2 Cl_2 + e^- occurs at the standard chlorine electrode potential[12,13],

$$Cl^- (aq) = 1/2\ Cl_2 + e^- @\ U_{SHE} = 1.36\ V \quad (1)$$

In this model, Gibbs free energy change (ΔG) at standard hydrogen electrode is given by[12]

$$\Delta G = \Delta E + \Delta E_{ZPE} - T\Delta S + \Delta G_U + \Delta G_{pH} \quad (2)$$

where ΔE, ΔE_{ZPE}, ΔS, and ΔG_U are the binding energy, change of zero-point energy, change of entropy, and electrode potential, respectively. T is the temperature (298.15 K). In addition, ΔG_{pH} =pH × $k_B T$ln10, where k_B is the Boltzmann constant.

The OER's 4-electron pathways in alkaline media can be given as follows:

$$* + OH^- \rightarrow *OH + e^- \quad (3)$$

$$*OH + OH^- \rightarrow *O + H_2O\ (l) + e^- \quad (4)$$

$$*O + OH^- \rightarrow *OOH + e^- \quad (5)$$

$$*OOH + OH^- \rightarrow * + O_2\ (g) + H_2O\ (l) + e^- \quad (6)$$

Therefore, the free-energy change of four reaction steps can be expressed as follows:

$$\Delta G_1 = G\ (*OH) + G\ (H_2)/2 + eU - G\ (*) - G\ (H_2O) \quad (7)$$

$$\Delta G_2 = G\ (*O) + G\ (H_2)/2 + eU - G\ (*OH) \quad (8)$$

$$\Delta G_3 = G\ (*OOH) + G\ (H_2)/2 + eU - G\ (*O) - G\ (H_2O) \quad (9)$$

$$\Delta G_4 = G\ (*) + G\ (H_2)/2 + eU + G\ (O_2) - G\ (*OOH) \quad (10)$$

where U is the potential measured against the normal hydrogen electrode under standard conditions. The theoretical overpotential for OER (η^{OER}) can be calculated by η^{OER} = max [ΔG_1, ΔG_2, ΔG_3, ΔG_4]/e − U_{eq}, where U_{eq} is the equilibrium potential.

The mechanism below containing two elementary steps was used for calculating the free-energy change for CER[13,14],

$$* + Cl^- \rightarrow *Cl + e^- \quad (11)$$

$$*Cl + 2OH^- \rightarrow OCl^- + H_2O + e^- \quad (12)$$

The adsorption energy of OH^- or Cl^- on the catalyst surface was determined using:

$$G_{ads} = G_{*A} - G_* - G_A,\ (A= Cl^- \text{ or } OH^-) \quad (13)$$

where the G_{*A} represents the free energy of the system after adsorption, G_* is the surface free energy, and G_A is the free energy of Cl^- or OH^-.

Molecular dynamic simulation details

For comparison, both Ir/NiFe LDH and NiFe LDH are built as the electrodes based on the models used in the DFT calculations. The solution model contains 1200 water molecules, 36 Na^+, 24 OH^-, and 12Cl^-. A vacuum layer with thickness of about 50 Å was added above the solution to exclude interactions between the neighboring images. The simulation box sizes are 22.6 × 28.0 × 130 Å^3 and 25.3 × 28.5 × 130 Å^3 for Ir/NiFe LDH and NiFe LDH electrodes, respectively. All the atoms in electrode model were fixed and the particles in solution model were free. The periodic boundary condition was set in all directions. Atom interactions were described by the 12-6 Lennard-Jones (LJ) and Columbic potentials. Water molecules were described by the SPC/E model[15].

The force fields of various ions were parameterized in previous studies[16,17]. The LJ parameters of electrodes were described by the INTERFACE-CVFF force field[18,19]. Furthermore, to describe the intense interaction between Ir surface and Cl^- in solution, Morse potential was employed as following:

$$E\ /\ kcal \cdot mol^{-1} = 100\left[e^{-4(r\ /\ \text{Å} - 2.78)} - 2e^{-2(r\ /\ \text{Å} - 2.78)}\right] \quad r < 5\ \text{Å}$$

in which *r* is the distance between Ir and Cl. Long-range electrostatic interactions were computed using the particle-particle particle-mesh (PPPM) algorithm with a root mean square accuracy of 10^{-4}. The cutoffs of Coulomb and Lennard-Jones interactions were 12.0 and 10.0 Å, respectively.

Molecular dynamic (MD) simulations were conducted using LAMMPS software package[20]. The energy of each simulation system was initially minimized with a tolerance of 10^{-5}. After minimization, the system temperature was controlled at 300 K by the Nosé-Hoover thermostat in the equilibrium simulations. After equilibrium, an external electric field of 0.1 V/Å was applied along z direction. The first 5 ns of each simulation were used for equilibration and the left 15 ns were collected for trajectory analysis with a time step of 1 fs.

Supplementary Notes

Supplementary Note 1. Calculations of AEM electrolyzer efficiency and electricity cost of hydrogen (6 M KOH seawater). The cost estimation includes only electricity consumption and follows the methodology reported in the literature.

H_2 production rate @ 0.5 A cm^{-2}
= (j A cm^{-2}) (1 e^-/1.602 × 10^{-19} C) (1 H_2/2 e^-)
= 0.5 A cm^{-2} / (1.602 × 10^{-19} C × 2) = 2.59 × 10^{-6} mol H_2 cm^{-2} s^{-1}

LHV of H_2
= 120 kJ g^{-1} H_2 = 2.42 × 10^5 J mol^{-1} H_2

H_2 power out
= (2.59 × 10^{-6} mol cm^{-2} s^{-1}) × (2.42 × 10^5 J mol^{-1}) = 0.627 W cm^{-2}

Electrolyzer Power @ 0.5 A cm^{-2} (6 M KOH seawater)
= (0.5 A cm^{-2}) (1.76V) = 0.88 W cm^{-2}

Efficiency of AEM
= (H_2 Power Out) / (Electrolyzer Power) = 0.627 W cm^{-2}/ 0.88W cm^{-2} = 71.2%

The molar mass of hydrogen gas is 2 g/mol. The mass of hydrogen gas produced by a 4 cm^2 electrode at a current density of 0.5 A·cm^{-2} within 1 hour
= (2.59 × 10^{-6} mol) × (2 g/mol) × 3600s × 4 cm^{-2} = 7.4592 × 10^{-5} kg/h H_2

Price per kilogram of hydrogen

= 1 kg H_2/H_2 production rate (4 cm^2) × Electrolyzer power × Electricity bill
= 1 kg / (7.4592 × 10^{-5} kg/h H_2) × (0.88 W cm^{-2} × 4 cm^2) × ($ 0.02 /kWh)
=$ 0.944 /kg H_2

Supplementary Figures

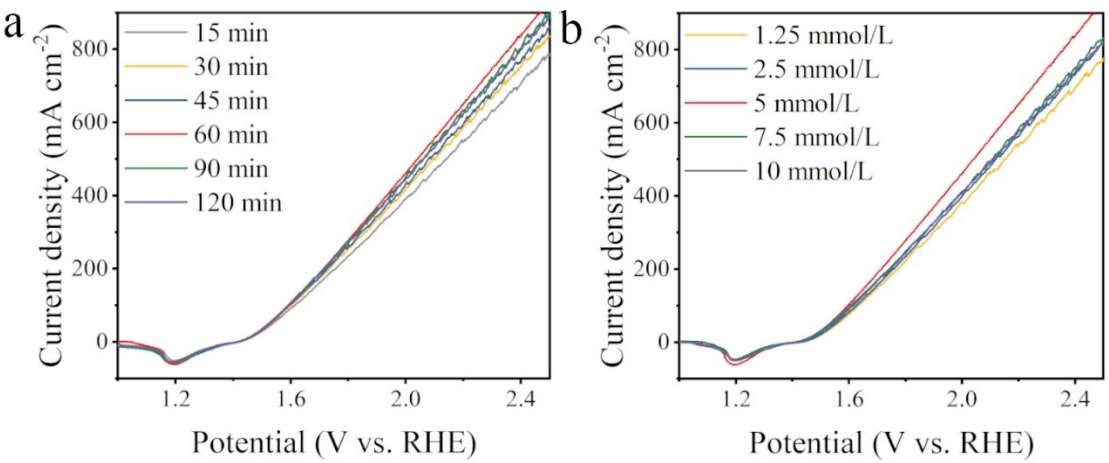

Fig. S1. (a) OER polarization curves of samples with different immersion times in $IrCl_3$ solution and (b) different $IrCl_3$ immersion concentrations, all measured without iR correction in 1 M KOH seawater.

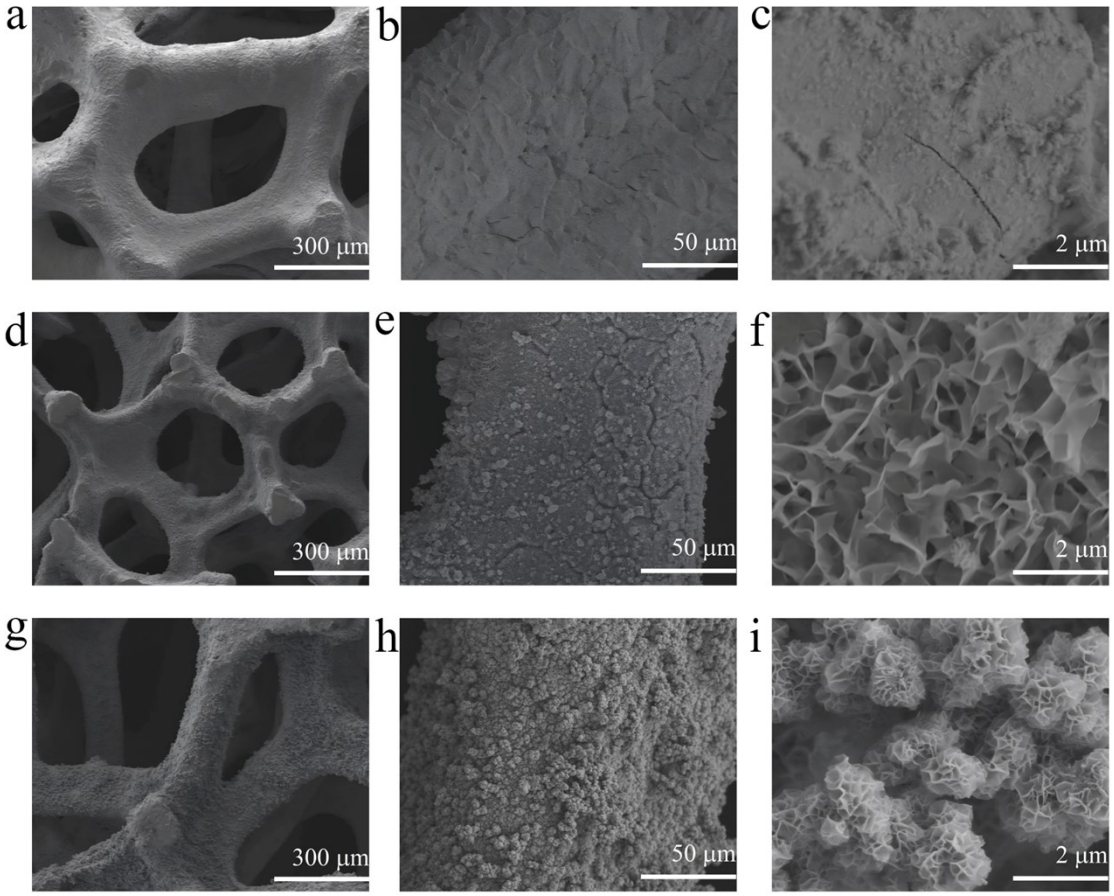

Fig. S2. SEM images of (a-c) Ir@IF, (d-f) NiFe LDH@IF, (g-i) Ir/NiFe LDH@IF.

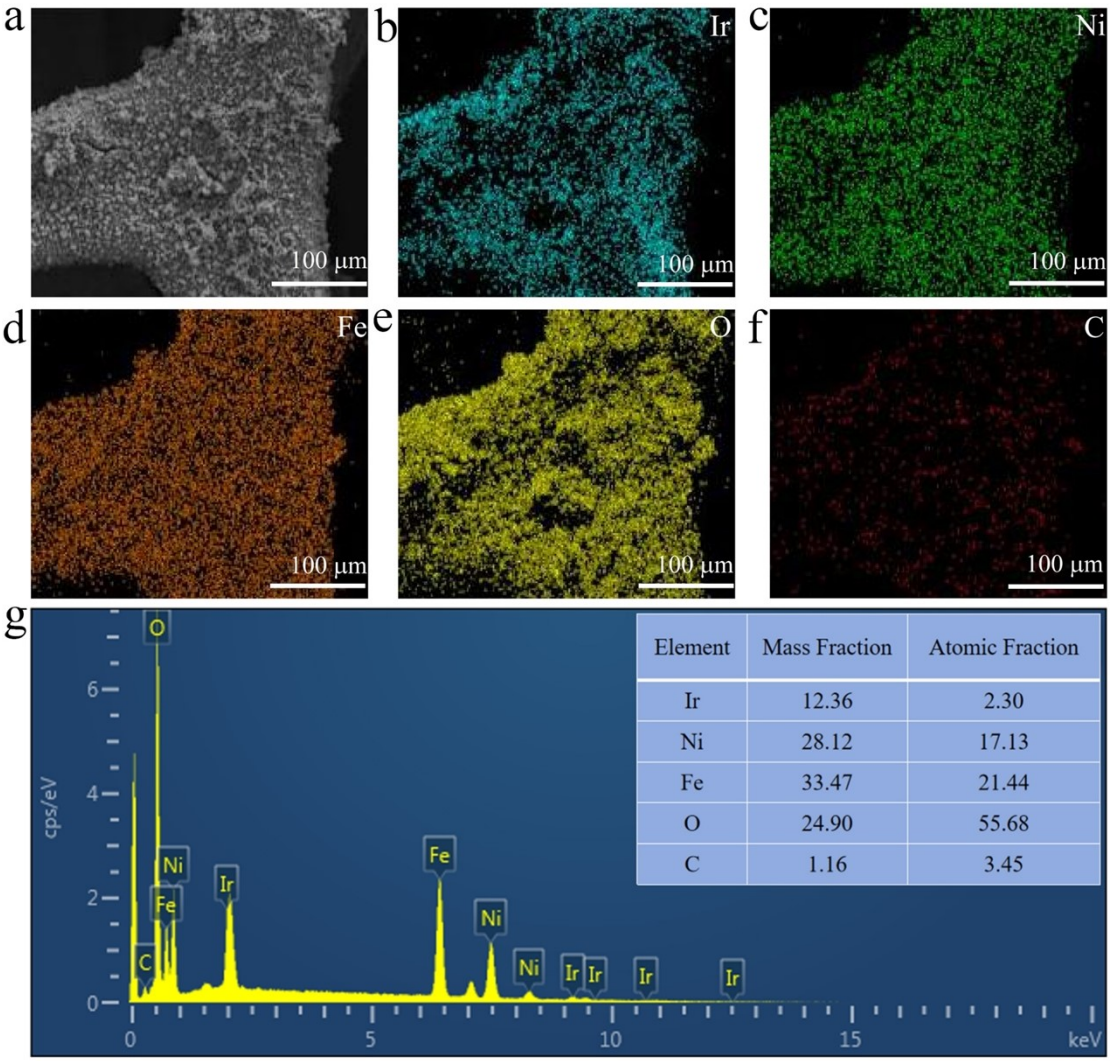

Element	Mass Fraction	Atomic Fraction
Ir	12.36	2.30
Ni	28.12	17.13
Fe	33.47	21.44
O	24.90	55.68
C	1.16	3.45

Fig. S3. (a-f) SEM-EDS images of Ir/NiFe LDH@IF. (g) SEM-EDX results of Ir/NiFe LDH@IF.

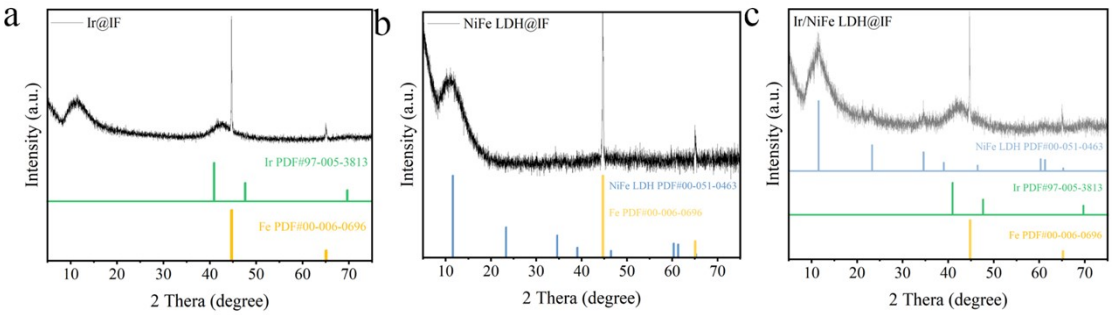

Fig. S4. XRD patterns of (a) Ir@IF, (b) NiFe LDH@IF and (c) Ir/NiFe LDH@IF.

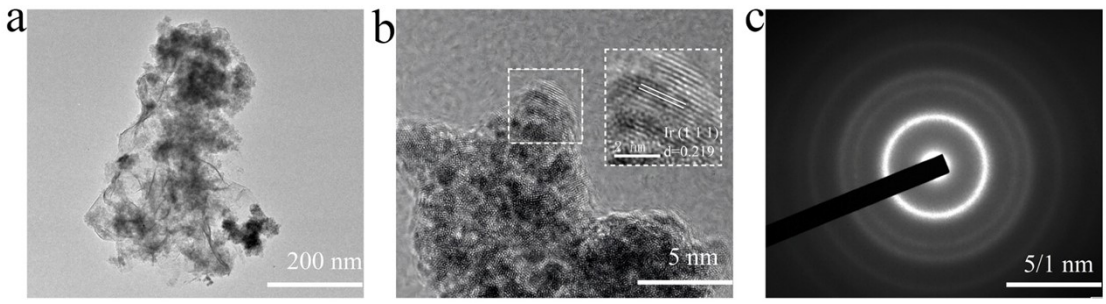

Fig. S5. (a) TEM image, (b) HRTEM image, (c) SAED pattern of Ir@IF.

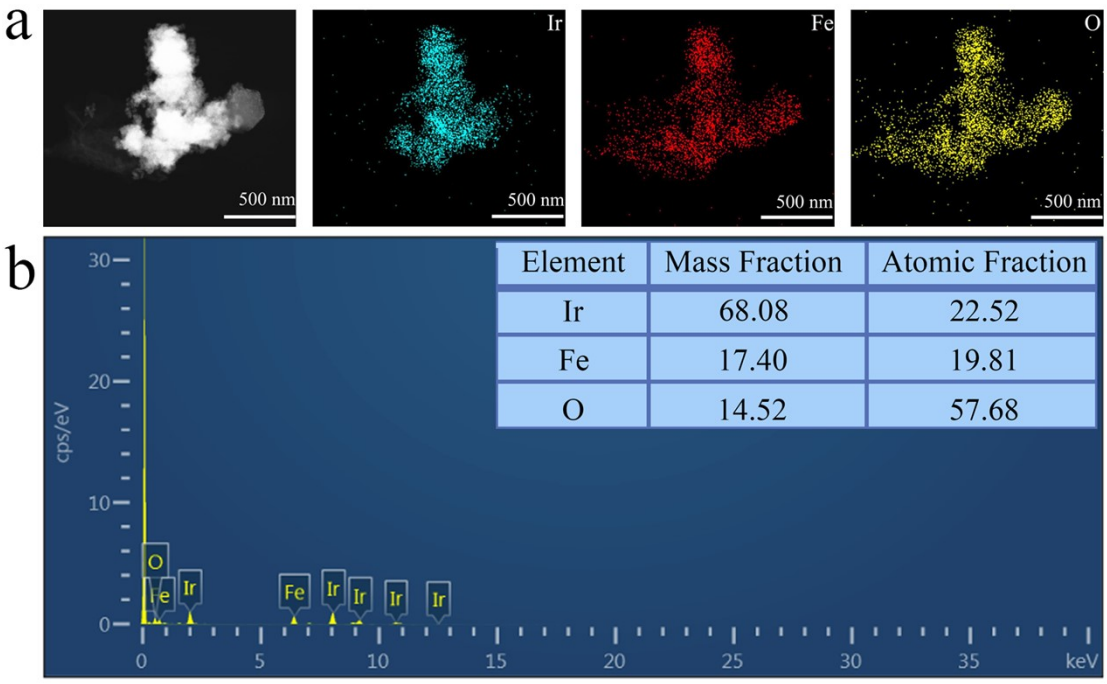

Fig. S6. (a) HAADF-STEM image for Ir@IF with elemental mapping images for Ir, Fe and O elements. (b) TEM-EDX results of Ir@IF.

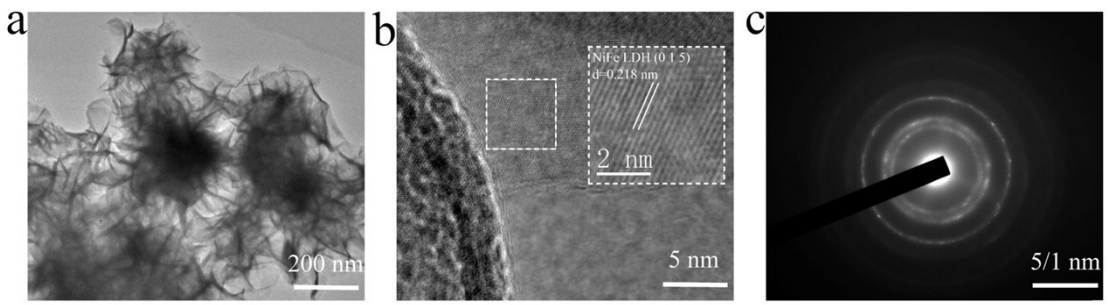

Fig. S7. (a) TEM image, (b) HRTEM image, (c) SAED pattern of NiFe LDH@IF.

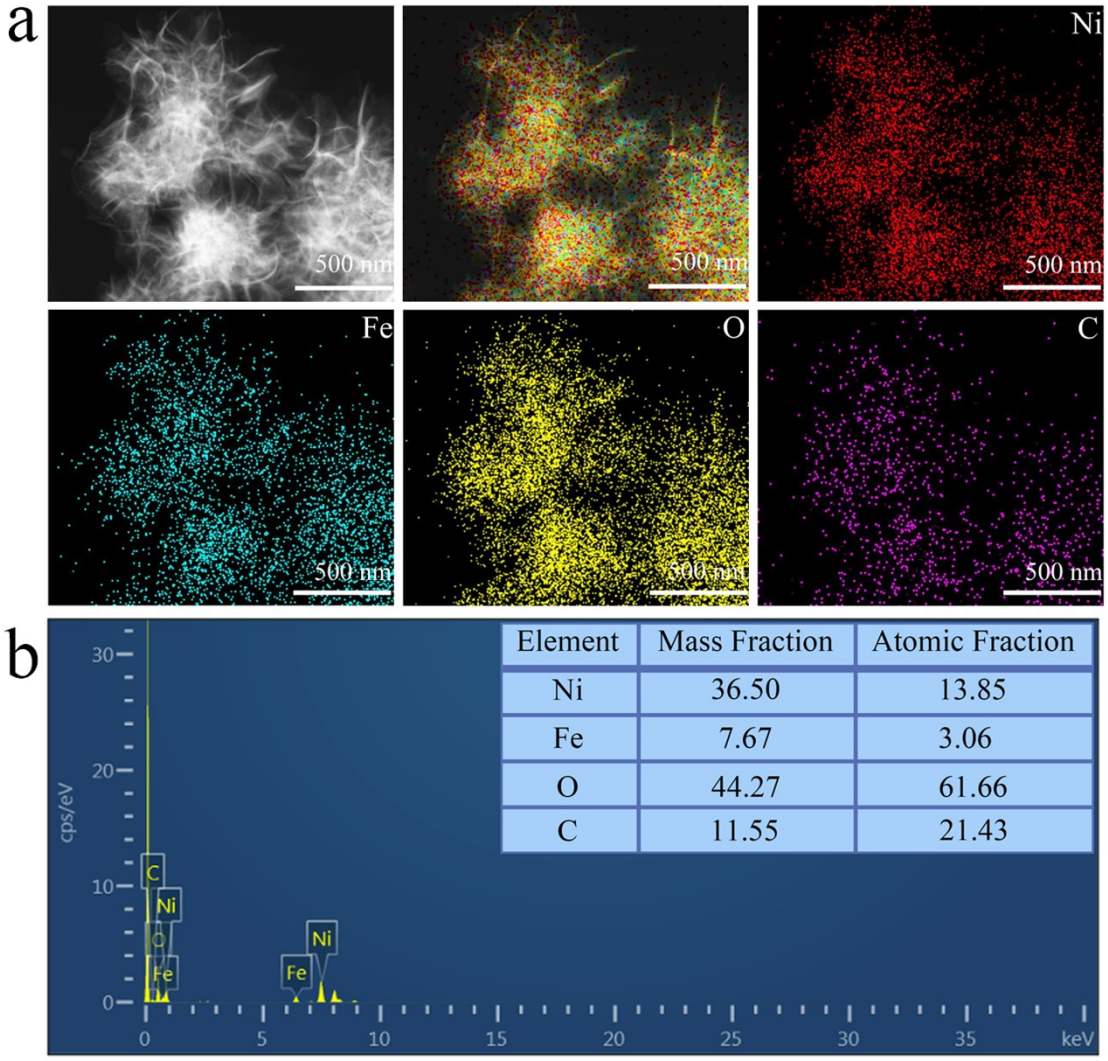

Fig. S8. (a) HAADF-STEM image for NiFe LDH@IF with elemental mapping images for Ni, Fe, O and C elements. (b) TEM-EDX results of NiFe LDH@IF.

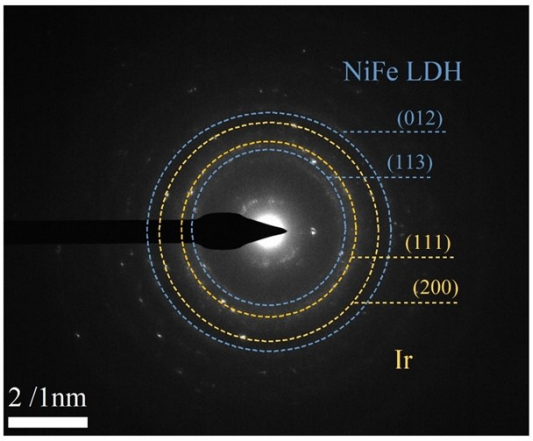

Fig. S9. SAED pattern of Ir/NiFe LDH@IF.

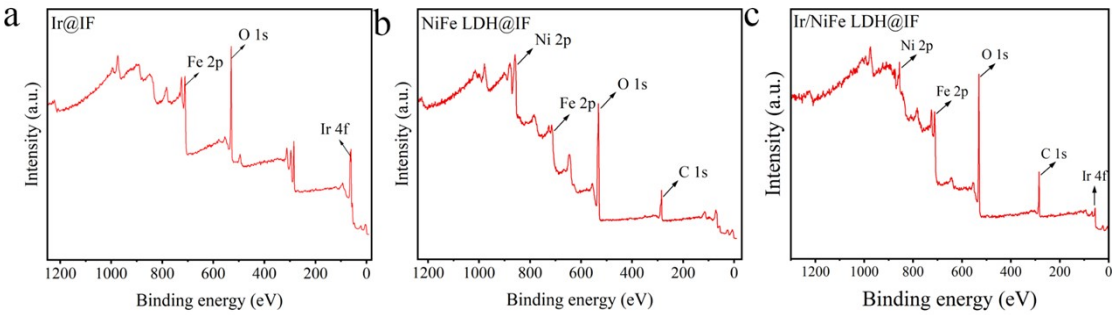

Fig. S10. XPS survey spectra of (a) Ir@IF, (b) NiFe LDH@IF, (c) Ir/NiFe LDH@IF.

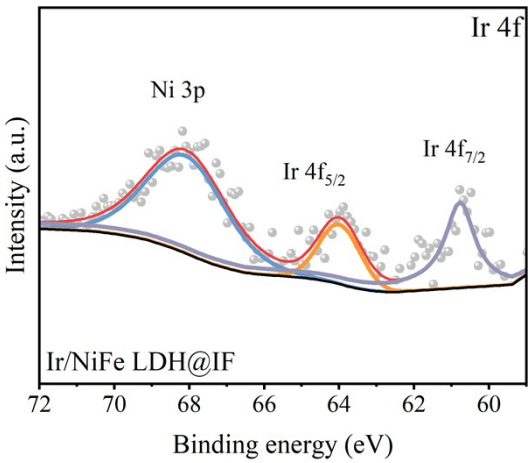

Fig. S11. Ir 4f high-resolution XPS spectra of Ir/NiFe LDH@IF.

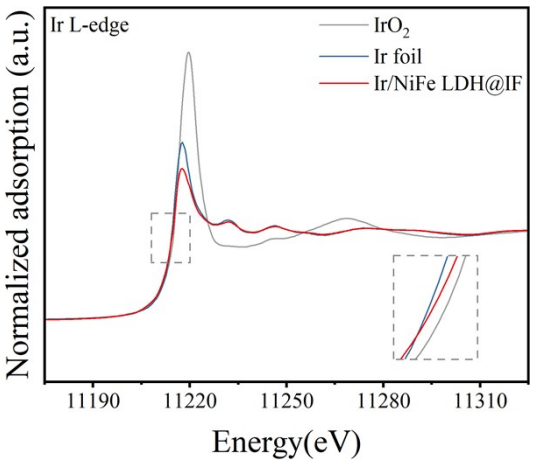

Fig. S12. Ir L_3-edge XANES spectra of Ir foil, IrO_2, and Ir/NiFe LDH@IF.

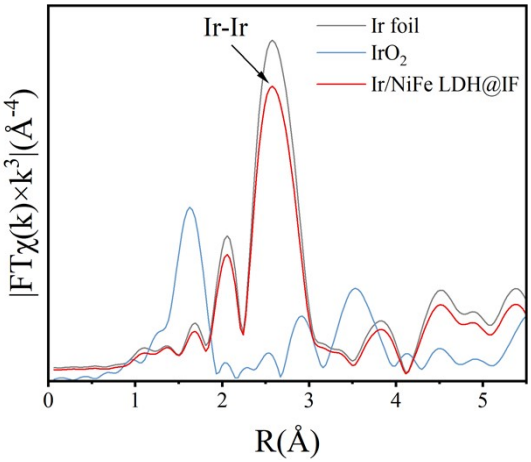

Fig. S13. Ir L_3-edge FT-EXAFS spectra of Ir foil, IrO_2, and Ir/NiFe LDH@IF.

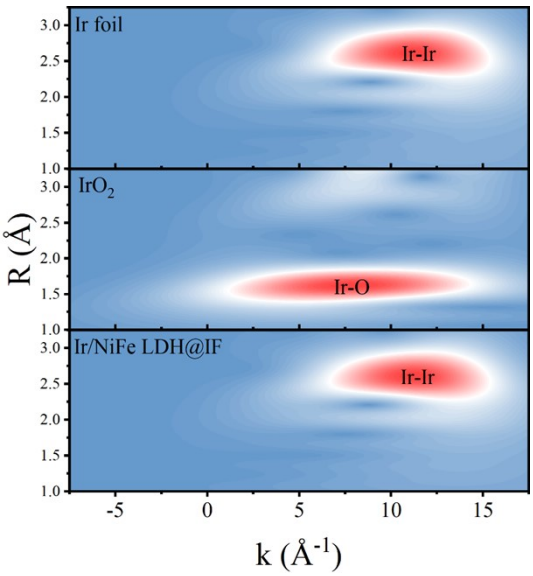

Fig. S14. Ir L_3-edge WT for the k^3-weighted EXAFS signals of Ir foil, IrO_2, and Ir/NiFe LDH@IF.

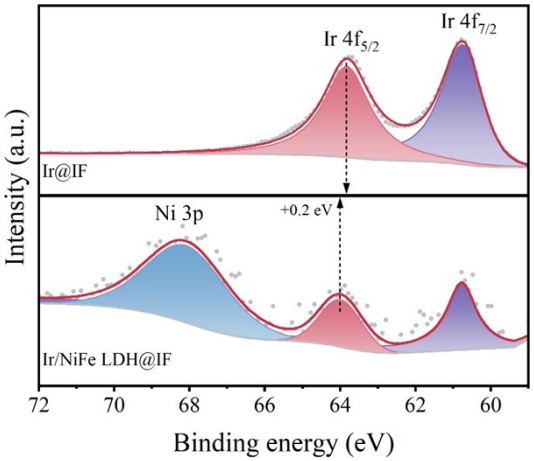

Fig. S15. XPS survey of Ir 4f XPS spectra of Ir@IF and Ir/NiFe LDH@IF.

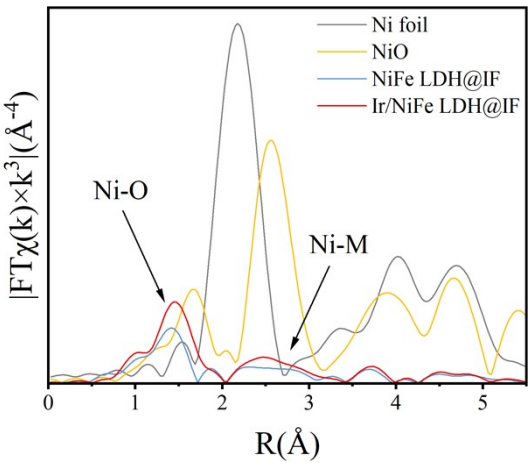

Fig. S16. Ni K-edge FT-EXAFS spectra of Ni foil, NiO, NiFe LDH@IF, and Ir/NiFe LDH@IF.

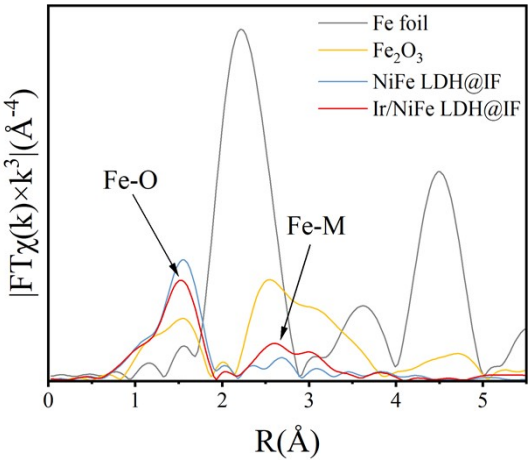

Fig. S17. Fe K-edge FT-EXAFS spectra of Fe foil, Fe_2O_3, NiFe LDH@IF, and Ir/NiFe LDH@IF.

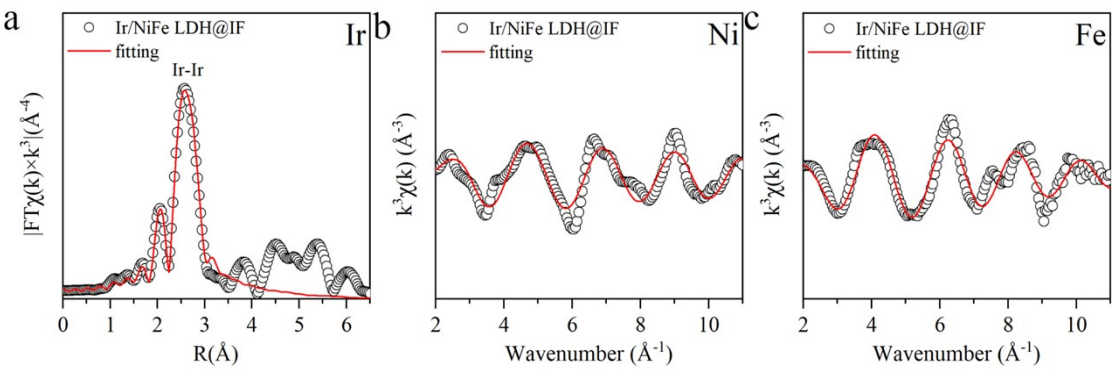

Fig. S18. k^3-weighted EXAFS spectra and fitting curves for Ir/NiFe LDH@IF are shown in (a) R-space at the Ir L_3-edge, (b) k-space at the Ni K-edge, and (c) k-space at the Fe K-edge.

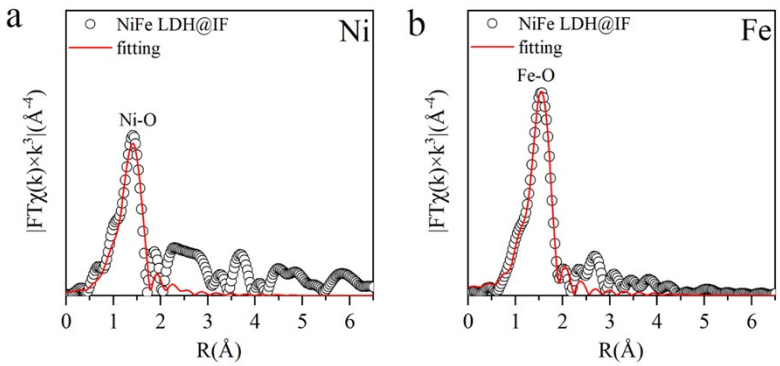

Fig. S19. k^3-weighted EXAFS spectra and fitting curves for NiFe LDH@IF are shown in (a) R-space at the Ni K-edge, and (b) R-space at the Fe K-edge.

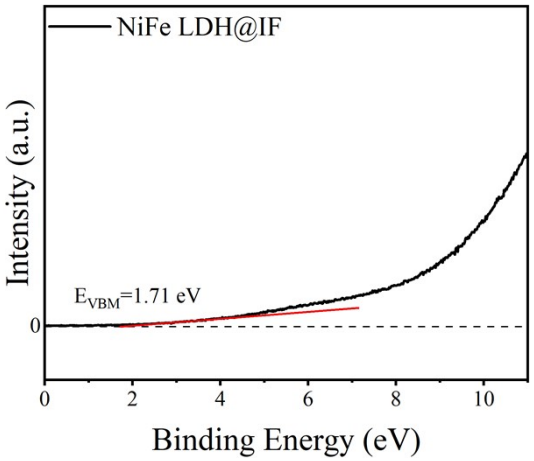

Fig. S20. UPS spectra of the VBM for NiFe LDH@IF.

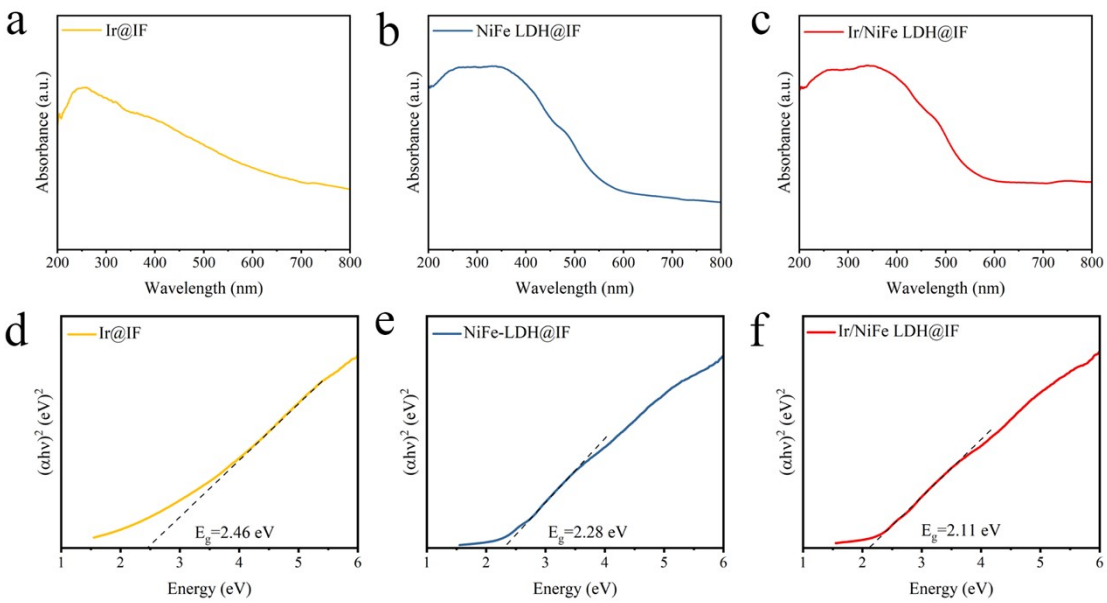

Fig. S21. UV-Vis diffuse reflectance spectra of (a) Ir@IF, (b) NiFe LDH@IF, and (c) Ir/NiFe LDH@IF. The corresponding Tauc plots of (d) Ir@IF, (e) NiFe LDH@IF, and (f) Ir/NiFe LDH@IF.

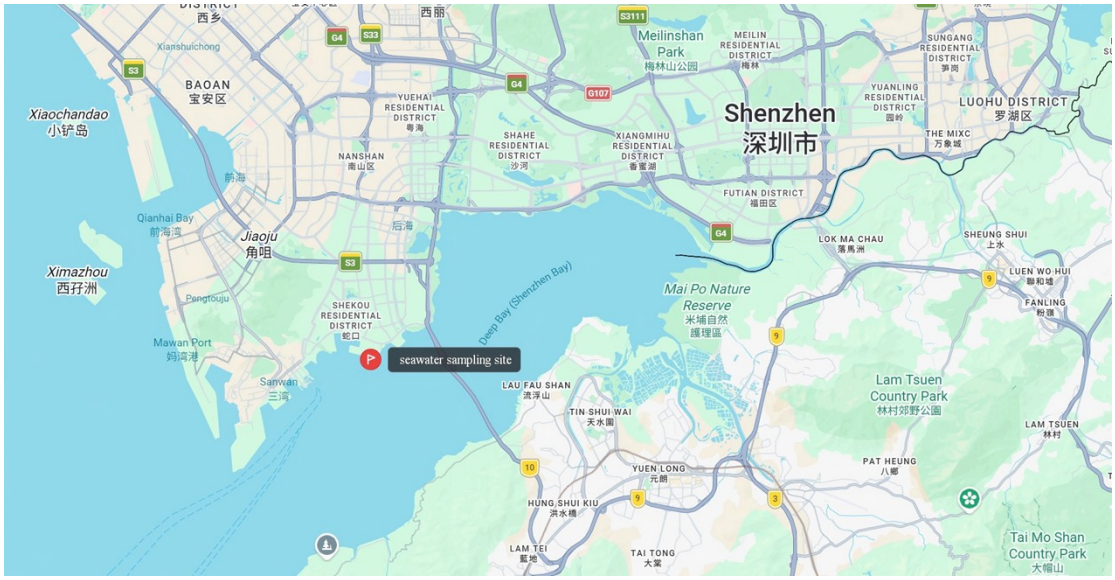

Fig. S22. The geographical location for the source of natural seawater.

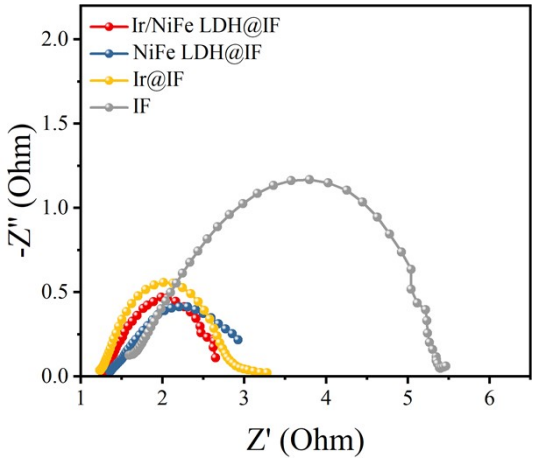

Fig. S23. Nyquist plots.

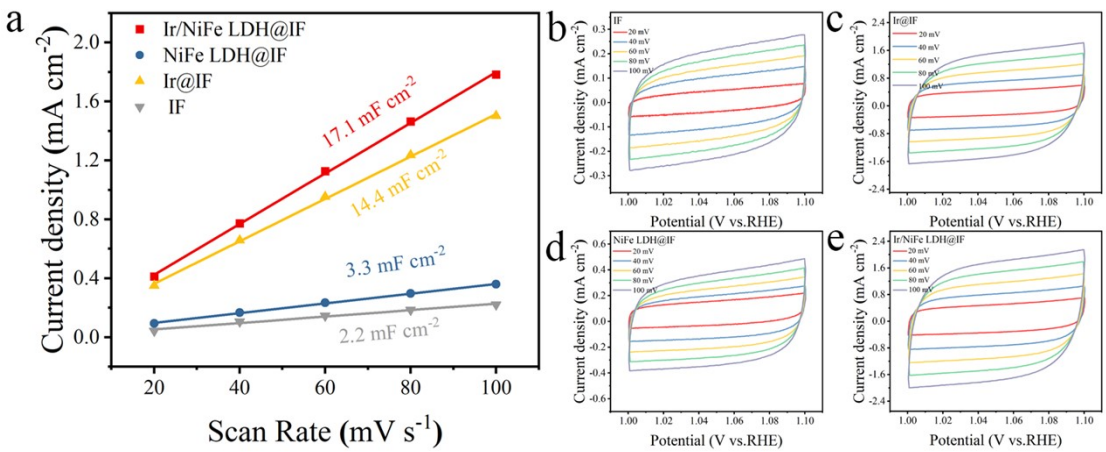

Fig. S24. The double-layer capacitance of (a) Ir/NiFe LDH@IF, NiFe LDH@IF, Ir@IF, and IF, and cyclic voltammograms of (b) IF, (c) Ir@IF, (d) NiFe LDH@IF, and (e) Ir/NiFe LDH@IF at scan rates in the range of 20-100 mV s^{-1} in alkaline seawater, respectively.

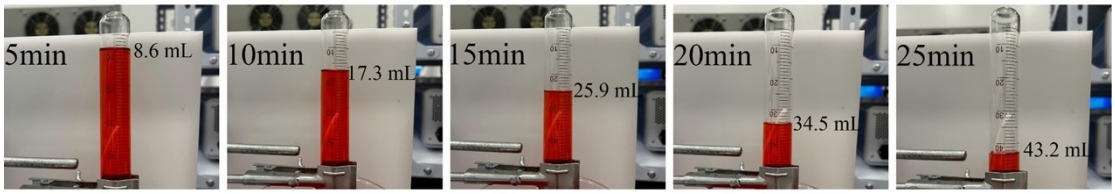

Fig. S25. Optical images of the drainage method for Ir/NiFe LDH@IF.

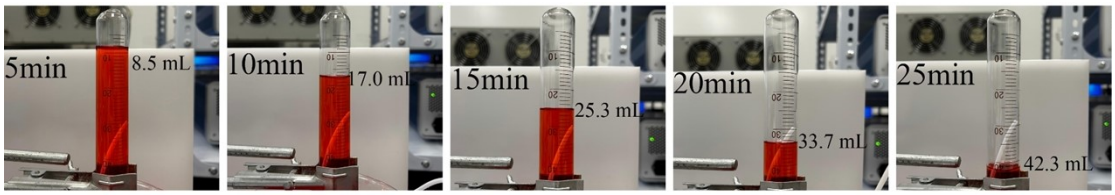

Fig. S26. Optical images of the drainage method for NiFe LDH@IF.

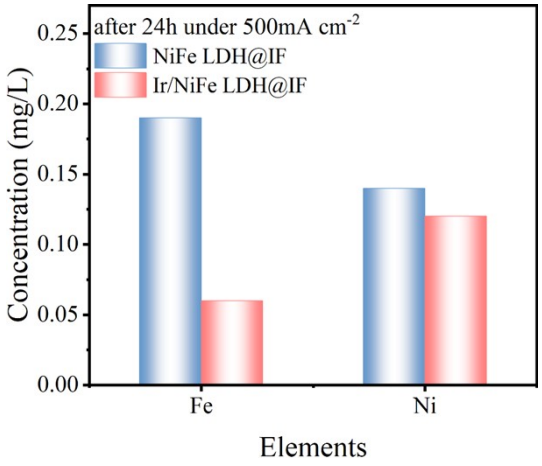

Fig. S27. ICP-OER results of electrolytes for NiFe LDH@IF and Ir/NiFe LDH@IF after OER process for 24 hours at 500 mA cm^{-2}.

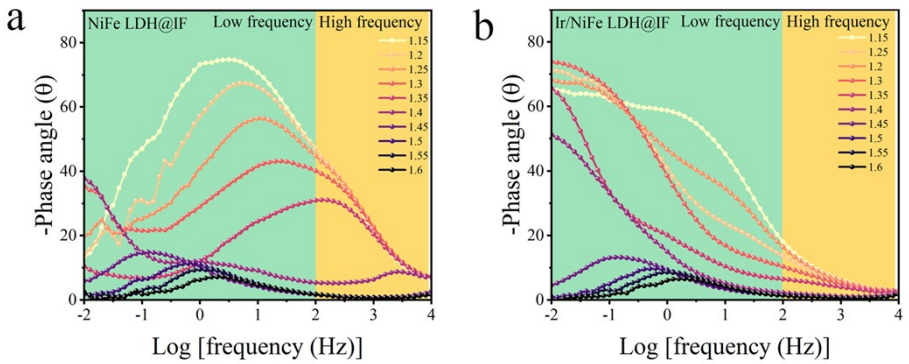

Fig. S28. Operando Bode phase angle plots of (a) NiFe LDH@IF and (b) Ir/NiFe LDH@IF in simulated alkaline seawater (1 M KOH + 0.5 M NaCl).

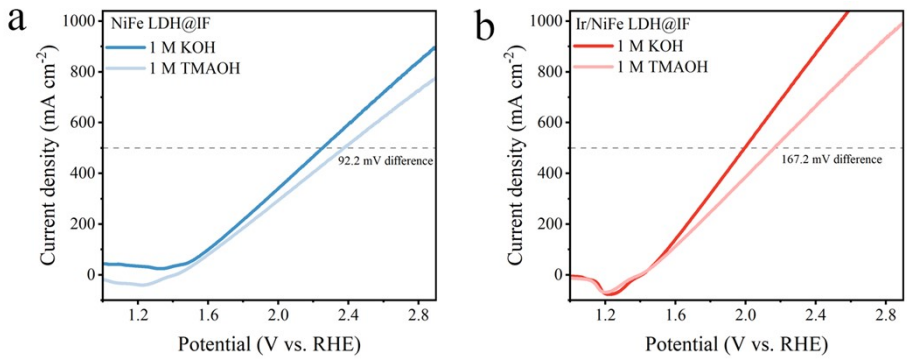

Fig. S29. Panels (a) and (b) are the LSV curves of NiFe LDH@IF and Ir/NiFe LDH@IF at different solutions, respectively. All measured without iR correction.

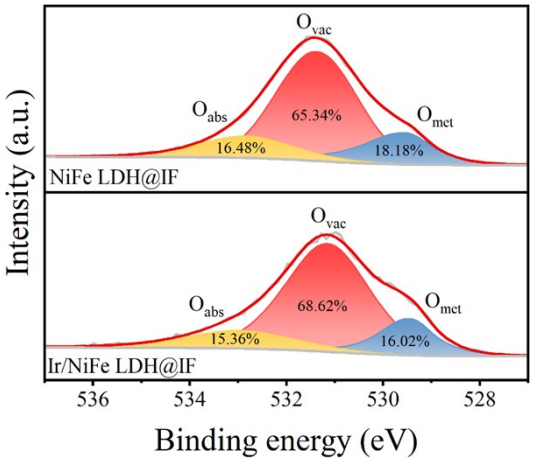

Fig. S30. O 1s XPS spectras of NiFe LDH@IF and Ir/NiFe LDH@IF.

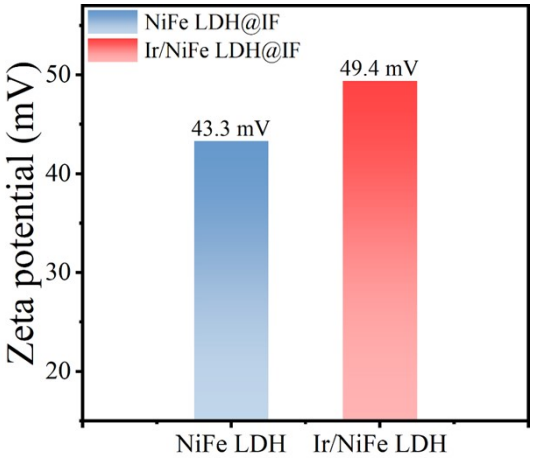

Fig. S31. The zeta potential of the Ir/NiFe LDH@IF and NiFe LDH@IF.

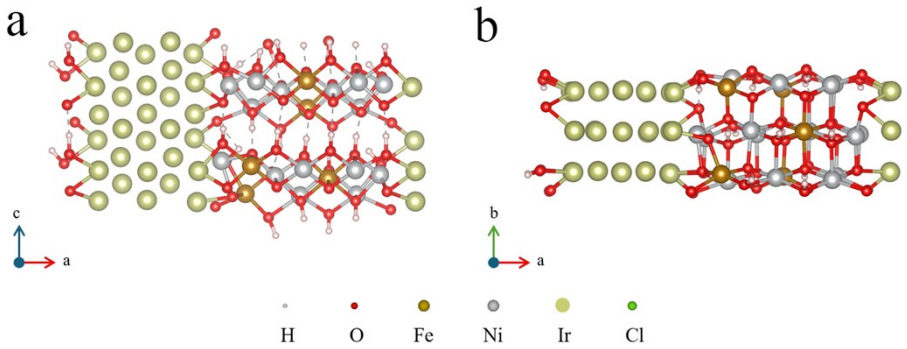

Fig. S32. Optimized configuration of the Ir/NiFe LDH interface derived from first-principles calculations. (a) top view and (b) side view.

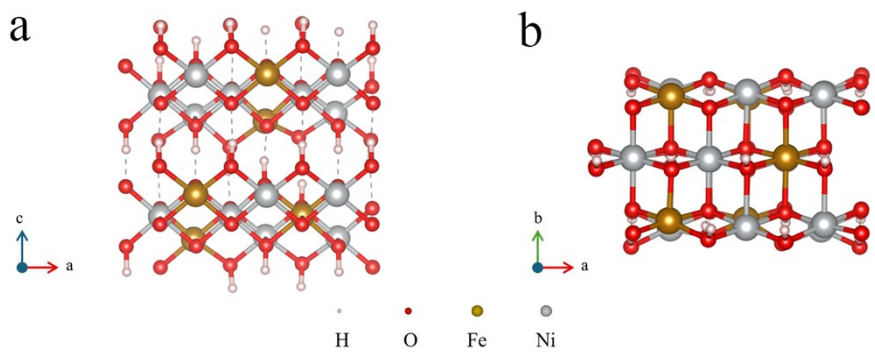

Fig. S33. Optimized configuration of the NiFe LDH interface derived from first-principles calculations. (a) top view and (b) side view.

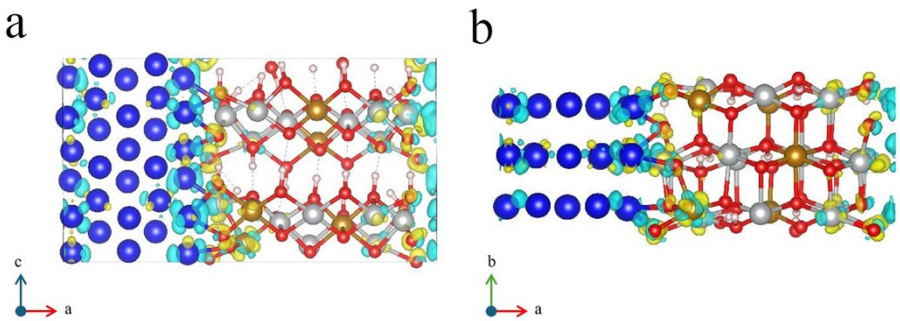

Fig. S34. Charge density difference of Ir/NiFe LDH. (a) top view and (b) side view.

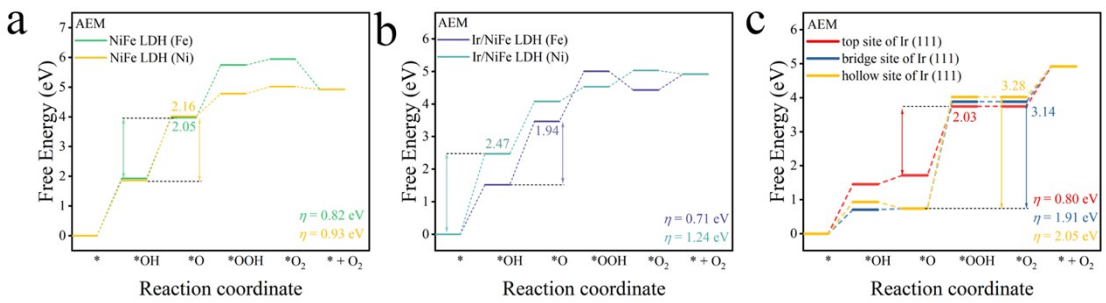

Fig. S35. Free energy diagrams for the OER following the AEM pathway on NiFe LDH and Ir/NiFe LDH: (a) Fe and Ni sites of NiFe LDH, (b) Ni and Fe sites of Ir/NiFe LDH, and (c) Ir sites of Ir/NiFe LDH.

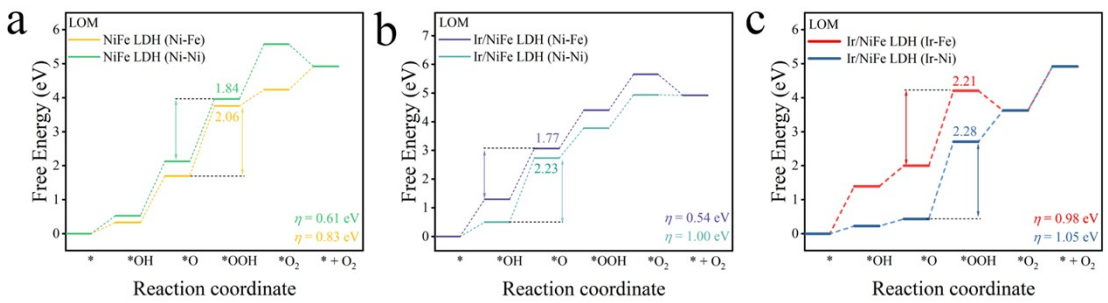

Fig. S36. Free energy diagrams for the OER following the LOM pathway on NiFe LDH and Ir/NiFe LDH: (a) Ni-Fe and Ni-Ni sites of NiFe LDH, (b) Ni-Fe and Ni-Ni sites of Ir/NiFe LDH, and (c) Ir-Fe and Ir-Ni sites of Ir/NiFe LDH.

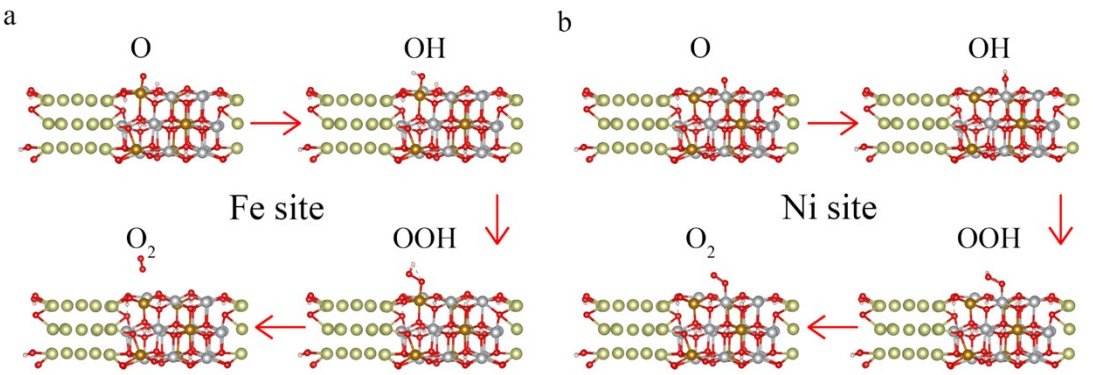

Fig. S37. Reaction pathway for the OER at (a) Fe sites and (b) Ni sites of Ir/NiFe LDH via the AEM mechanism.

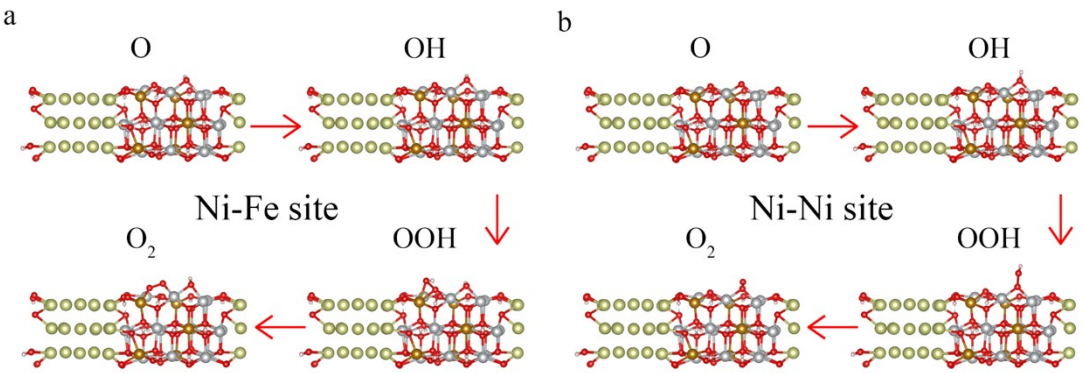

Fig. S38. Reaction pathway for the OER at (a) Ni-Fe sites and (b) Ni-Ni sites of Ir/NiFe LDH via the LOM mechanism.

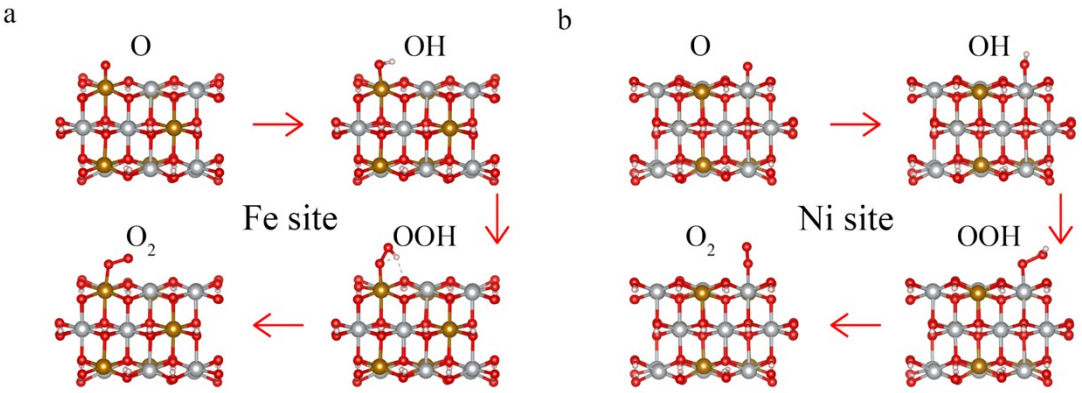

Fig. S39. Reaction pathway for the OER at (a) Fe sites and (b) Ni sites of NiFe LDH via the AEM mechanism.

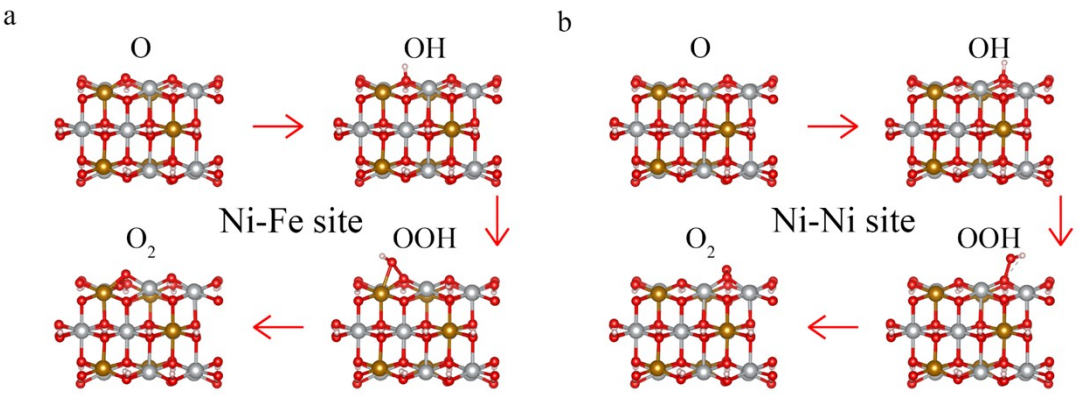

Fig. S40. Reaction pathway for the OER at (a) Ni-Fe sites and (b) Ni-Ni sites of NiFe LDH via the LOM mechanism.

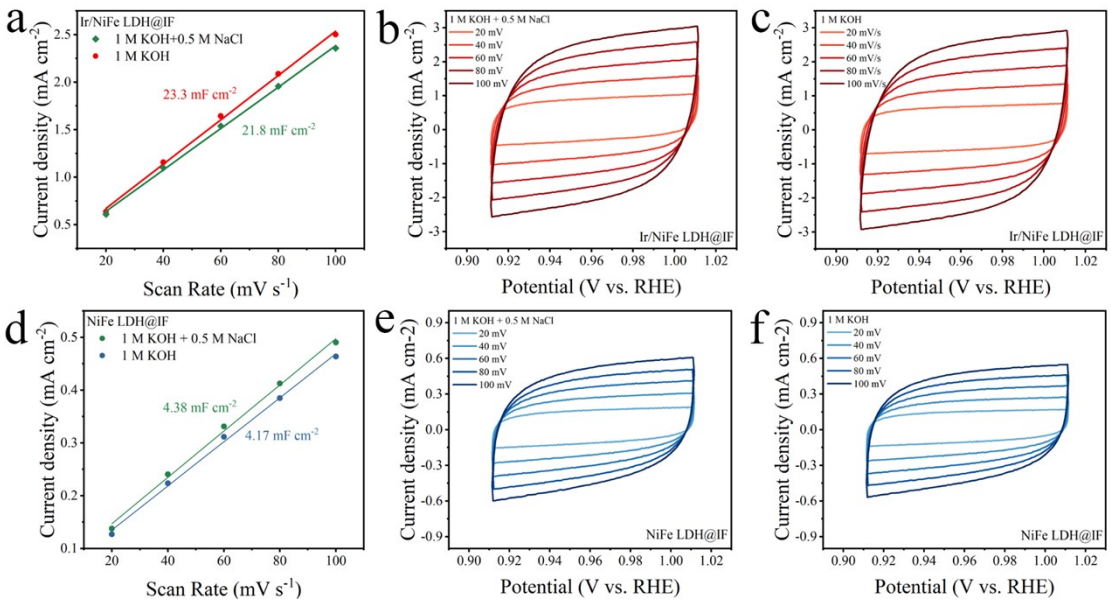

Fig. S41. (a-f) CV curves and corresponding calculation of C_{dl} of Ir/NiFe LDH@IF and NiFe LDH@IF in alkaline electrolyte and alkaline saline electrolyte. The scan rates ranging from 20 mV s^{-1} to 100 mV s^{-1}.

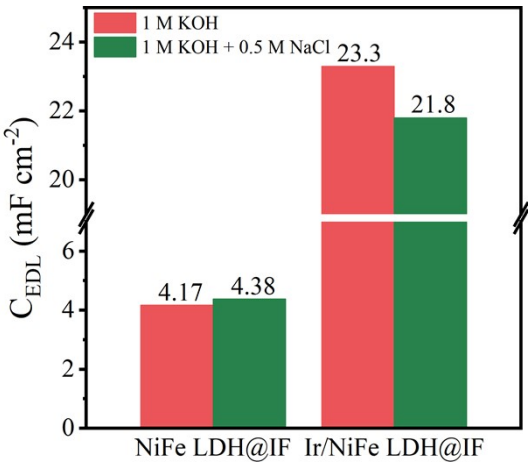

Fig. S42. Experimental C_{dl} values in 1 M KOH and 1 M KOH + 0.5 M NaCl.

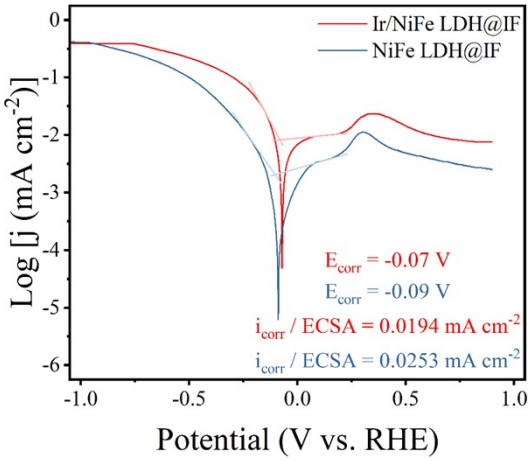

Fig. S43. Corrosion behavior curves of Ir/NiFe LDH@IF and NiFe LDH@IF in alkaline seawater.

Corrosion-related Tafel analysis reveals a positive shift in the corrosion potential (E_{corr}) from -0.09 V for NiFe LDH@IF to -0.07 V for Ir/NiFe LDH@IF, indicating improved thermodynamic resistance to corrosion. After normalization to the ECSA, the corrosion current density decreases from 0.0253 mA cm^{-2} for NiFe LDH@IF to 0.0194 mA cm^{-2} for Ir/NiFe LDH@IF, suggesting a lower intrinsic corrosion tendency of the heterostructure.

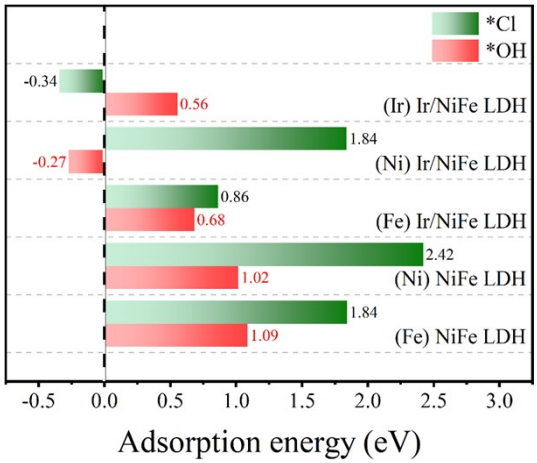

Fig. S44. Calculated Cl^- adsorption energies at different sites.

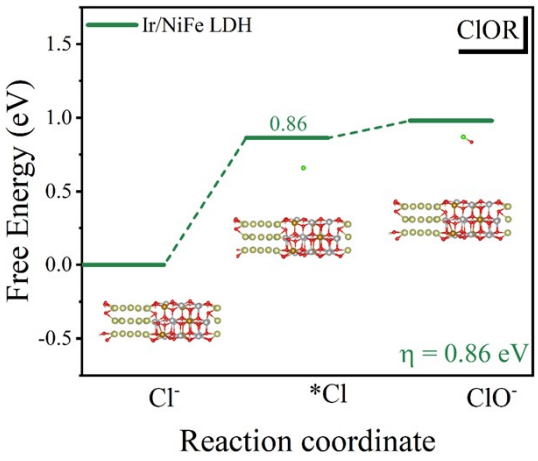

Fig. S45. Free energy diagrams for ClOR on Ir/NiFe LDH.

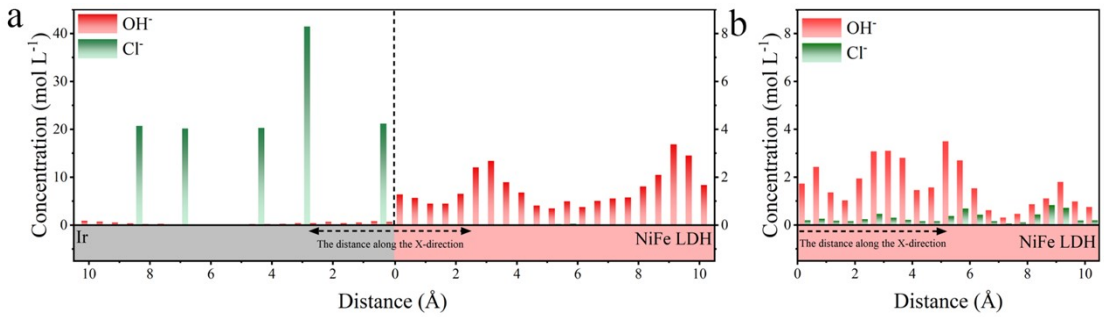

Fig. S46. (a) OH^- and Cl^- concentration profiles along the x-direction for the Ir/NiFe LDH electrode (Ir surface and NiFe LDH surface). (b) OH^- and Cl^- concentration profiles along the x-direction on the NiFe LDH electrode surface.

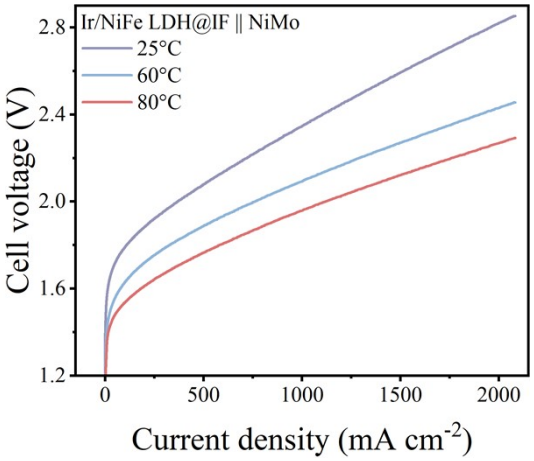

Fig. S47. Polarization curves of AEM electrolyzers with Ir/NiFe LDH@IF || NiMo at different temperatures.

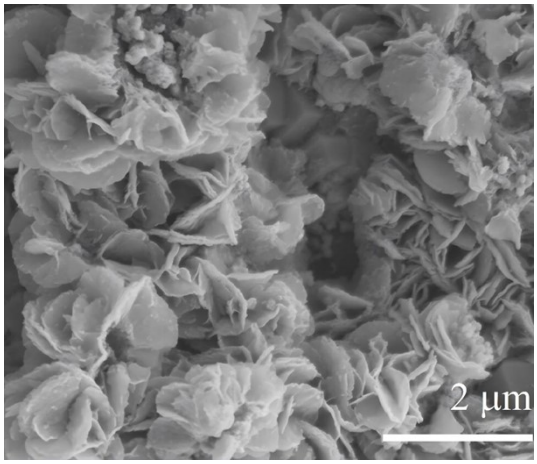

Fig. S48. SEM image of the OER-side Ir/NiFe LDH@IF after the long-term (5200 h) AEM device stability testing.

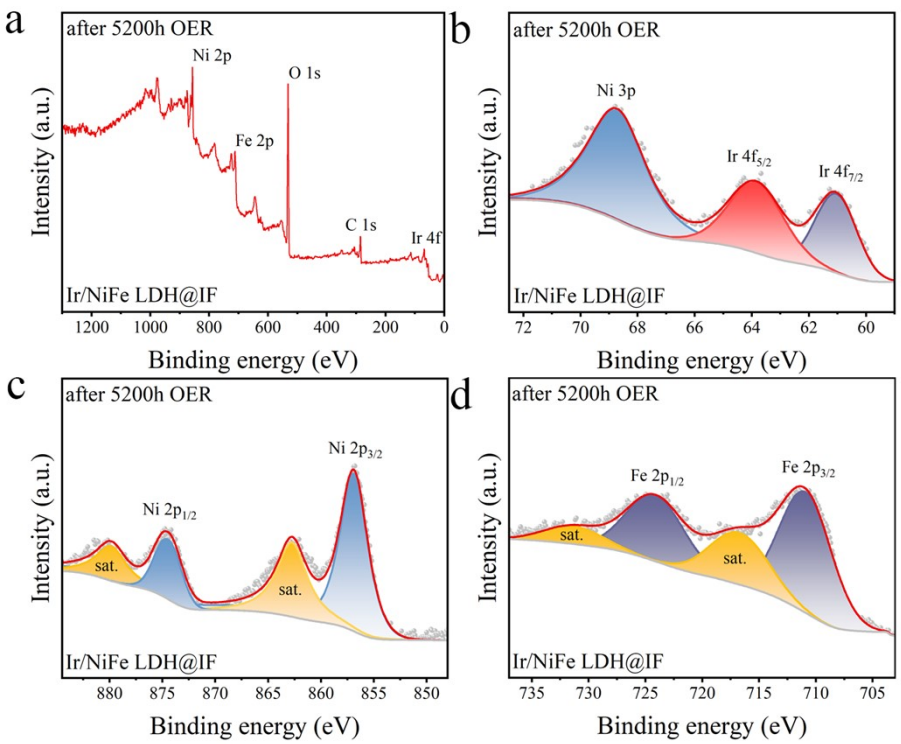

Fig. S49. (a) XPS survey spectra, and high-resolution XPS spectra of (b) Ir 4f, (c) Ni 2p, and (d) Fe 2p of Ir/NiFe LDH@IF on the OER side before and after the long-term (5200 h) AEM device stability testing.

Supplementary Tables

Table S1. ICP-OES results of pristine Ir/NiFe LDH@IF.

	Element	Mass Fraction
Ir/NiFe LDH@IF	Ir	0.39 %
	Ni	1.29 %
	Fe	46.64 %

Table S2. EXAFS fitting parameters at the Ir L_3-edge for various samples.

Sample	Shell	CN[a]	R(Å)[b]	σ^2 (Å^2)[c]	ΔE_0(eV)[d]	R factor
Ir foil	Ir-Ir	12.0*	2.71±0.01	0.0037	8.4	0.0028
IrO_2	Ir-O	6.0*	1.98±0.01	0.0019	11.2	0.0133
Ir/NiFe LDH@IF	Ir-Ir	10.1±0.6	2.71±0.01	0.0036	8.2	0.0026

(a) CN, coordination number; (b) R, distance between absorber and backscatter atoms; (c) σ^2, Debye-Waller factor to account for both thermal and structural disorders; (d) ΔE (0), inner potential correction; R factor indicates the goodness of the fit. S_0^2 was fixed to 0.905, according to the experimental EXAFS fit of Ir foil by fixing CN as the known crystallographic value. A reasonable range of EXAFS fitting parameters: $0.700 < S_0^2 < 1.000$; CN > 0; σ^2Å$^2 > 0$; $|\Delta E_0| < 15$ eV; R factor < 0.02.

Table S3. EXAFS fitting parameters at the Fe K-edge for various samples.

Sample	Shell	CN[a]	R(Å)[b]	σ^2 (Å^2)[c]	ΔE_0(eV)[d]	R factor
Fe foil	Fe-Fe	8.0*	2.48±0.01	0.0055	7.5	0.0028
	Fe-Fe	6.0*	2.85±0.01	0.0072	6.6	
Fe_2O_3	Fe-O	6.0*	1.99±0.01	0.0080	-2.0	0.0192
	Fe-Fe	8.0*	2.95±0.01	0.0069	-3.4	
	Fe-Fe	4.0*	3.43±0.01	0.0019	11.6	
Ir/NiFe LDH@IF	Fe-O	5.7±0.1	1.99±0.01	0.0066	-3.4	0.0019
NiFe LDH@IF	Fe-O	5.9±0.1	2.00±0.01	0.0053	-2.0	0.0018

Table S4. EXAFS fitting parameters at the Ni K-edge for various samples.

Sample	Shell	CN[a]	R(Å)[b]	σ^2 (Å^2)[c]	ΔE_0(eV)[d]	R factor
Ni foil	Ni-Ni	12.0*	2.48±0.01	0.0062	6.4	0.0011
NiO	Ni-O	6.0*	2.08±0.01	0.0058	-1.5	0.0059
	Ni-Ni	12.0*	2.95±0.01	0.0062	-4.5	
Ir/NiFe LDH@IF	Ni-Ni	2.6±0.2	1.86±0.01	0.0025	3.5	0.0151
NiFe LDH@IF	Ni-Ni	2.9±0.3	1.85±0.01	0.0071	-3.5	0.0185

Table S5. Operating parameters of the AEM-WE.

Anode catalyst	Ir/NiFe LDH@IF
Anode area	2×2 cm (4 cm^2)
Cathode catalyst	Commercial NiMo alloy
Cathode area	2×2 cm (4 cm^2)
AEM membrane	Fumasep FAA-3-PK-130
Electrolyte	6 M KOH + seawater
Operating temperature	25-80 °C

Table S6. Calculations of AEM electricity cost of hydrogen.

	Operating current density (mA cm^{-2})	EE (%)	Electricity cost of H_2 (USD $/kg)	Electricity expense (kWh Nm^{-3})
Ir/NiFe LDH@IF	500	71.2	0.944	4.21
	1000	64.0	1.051	4.69
	1500	59.1	1.137	5.07
	2000	55.5	1.211	5.41

Table S7. The stability current density, corresponding cell voltage, and operational lifetime of Ir/NiFe LDH@IF and the most advanced OER catalyst were compared in alkaline seawater electrolyzers.

Electrocatalysts	Potential (V)	Operating current density (mA cm^{-2})	Time (h)	Reference
Ir/NiFe LDH@IF	2.08 V	500	5200	This work
NiFe-LDH@Ag	1.95 V	400	1200	[21]
NFCP	1.70 V	500	320	[22]
Fe-L-MoS_2	2.476 V	200	170	[23]
CoFe-Ci@GQDs/NF	-	442	200	[24]
Os-Ni_4Mo/MoO_2	-	200	200	[25]
RuMoNi	-	500	240	[26]
(NiFe)C_2O_4/NF	2.4 V	500	150	[27]
NFB-LDH	1.98 V	400	100	[28]
(Ni,Fe)S_2@Ti_3C_2	1.80 V	500	500	[29]
CoCe-O-Ir_{SA}	1.92 V	500	150	[30]
FeMoOOH/NF	-	500	40	[31]
Ni_3FeN@PO_4^{3-}/NF	1.95 V	500	200	[32]
NiFeLDH-FLPs	-	200	250	[33]
$Ni(OH)_2$/L-LFP	-	250	100	[34]
CrO_4^{2-}-NiFe LDH/Cr_2O_3	-	500	200	[35]
$Fe_4N/Co_3N/MoO_2$	1.63 V	500	200	[36]
Ru-BO_x-OH-300	1.73 V	500	200	[37]
Fe-Ni_2Pv	1.63 V	200	100	[38]
Cr_2O_3-CoO_x	-	500	100	[39]
Fe-$Ni(OH)_2$	1.70 V	200	250	[40]
Pt_{SA}-$Ni_{6.6}Fe_{0.4}P_3$	1.46 V	100	120	[41]
MoO_3@CoO/CC	1.81 V	1000	500	[42]
NiFe LDH-[PO_4^{3-}]	2.0 V	1000	1000	[43]
NiFe LDH/NF with PF_6^-	2.02 V	1000	1000	[44]
Ir/CoFe-LDH	-	1000	2000	[45]
CoFeAl-LDH	2.06 V	1000	500	[46]

References

1 W. Kohn and L. J. Sham, *Phys. Rev.*, 1965, **140**, A1133–A1138.
2 G. Kresse and J. Furthmüller, *Phys. Rev. B*, 1996, **54**, 11169–11186.
3 P. E. Blöchl, *Phys. Rev. B*, 1994, **50**, 17953–17979.
4 J. P. Perdew, K. Burke and M. Ernzerhof, *Phys. Rev. Lett.*, 1996, **77**, 3865–3868.
5 Y. Mei, J. Chen, Q. Wang, Y. Guo, H. Liu, W. Shi, C. Lin, Y. Yuan, Y. Wang, B. Y. Xia and Y. Yao, *Sci. Adv.*, 2024, **10**, eadq6758.
6 S. Grimme, J. Antony, S. Ehrlich and H. Krieg, *J. Chem. Phys.*, 2010, **132**, 154104.
7 H. J. Monkhorst and J. D. Pack, *Phys. Rev. B*, 1976, **13**, 5188–5192.
8 E. Sanville, S. D. Kenny, R. Smith and G. Henkelman, *J. Comput. Chem.*, 2007, **28**, 899–908.
9 A. Hjorth Larsen, J. Jørgen Mortensen, J. Blomqvist, I. E. Castelli, R. Christensen, M. Dułak, J. Friis, M. N. Groves, B. Hammer, C. Hargus, E. D. Hermes, P. C. Jennings, P. Bjerre Jensen, J. Kermode, J. R. Kitchin, E. Leonhard Kolsbjerg, J. Kubal, K. Kaasbjerg, S. Lysgaard, J. Bergmann Maronsson, T. Maxson, T. Olsen, L. Pastewka, A. Peterson, C. Rostgaard, J. Schiøtz, O. Schütt, M. Strange, K. S. Thygesen, T. Vegge, L. Vilhelmsen, M. Walter, Z. Zeng and K. W. Jacobsen, *J. Phys. Condens. Matter*, 2017, **29**, 273002.
10 J. K. Nørskov, J. Rossmeisl, A. Logadottir, L. Lindqvist, J. R. Kitchin, T. Bligaard and H. Jónsson, *J. Phys. Chem. B*, 2004, **108**, 17886–17892.
11 P. Prabhu, V.-H. Do, T. Yoshida, Y. Zhou, H. Ariga-Miwa, T. Kaneko, T. Uruga, Y. Iwasawa and J.-M. Lee, *ACS Nano*, 2024, **18**, 9942–9957.
12 H. A. Hansen, I. C. Man, F. Studt, F. Abild-Pedersen, T. Bligaard and J. Rossmeisl, *Phys Chem Chem Phys*, 2010, **12**, 283–290.
13 Y. Yu, W. Zhou, X. Zhou, J. Yuan, X. Zhang, L. Wang, J. Li, X. Meng, F. Sun, J. Gao and G. Zhao, *ACS Catal.*, 2024, **14**, 18322–18332.
14 Y. Liu, C. Li, C. Tan, Z. Pei, T. Yang, S. Zhang, Q. Huang, Y. Wang, Z. Zhou, X. Liao, J. Dong, H. Tan, W. Yan, H. Yin, Z.-Q. Liu, J. Huang and S. Zhao, *Nat. Commun.*, 2023, **14**, 2475.
15 H. J. C. Berendsen, J. R. Grigera and T. P. Straatsma, *J. Phys. Chem.*, 1987, **91**, 6269–6271.
16 F. Liu and D. Sun, *ACS Omega*, 2019, **4**, 18692–18698.
17 D. J. Bonthuis, S. I. Mamatkulov and R. R. Netz, *J. Chem. Phys.*, 2016, **144**, 104503.
18 H. Heinz, T.-J. Lin, R. Kishore Mishra and F. S. Emami, *Langmuir*, 2013, **29**, 1754–1765.
19 K. Kanhaiya, S. Kim, W. Im and H. Heinz, *Npj Comput. Mater.*, 2021, **7**, 17.
20
21 W. Xu, Z. Wang, P. Liu, X. Tang, S. Zhang, H. Chen, Q. Yang, X. Chen, Z. Tian, S. Dai, L. Chen and Z. Lu, *Adv. Mater.*, 2024, **36**, 2306062.
22 Y. Yu, W. Zhou, X. Zhou, J. Yuan, X. Zhang, L. Wang, J. Li, X. Meng, F. Sun, J. Gao and G. Zhao, *ACS Catal.*, 2024, **14**, 18322–18332.
23 Z. Li, W. Tao, Y. Wang, X. Ye, Y. Chen, B. Han and L. Y. S. Lee, *J. Am. Chem. Soc.*, 2025, **147**, 24461–24472.

24 R. Fan, C. Liu, Z. Li, H. Huang, J. Feng, Z. Li and Z. Zou, *Nat. Sustain.*, 2024, **7**, 158–167.
25 D. Liu, X. Wei, J. Lu, X. Wang, K. Liu, Y. Cai, Y. Qi, L. Wang, H. Ai and Z. Wang, *Adv. Mater.*, 2024, **36**, 2408982.
26 X. Kang, F. Yang, Z. Zhang, H. Liu, S. Ge, S. Hu, S. Li, Y. Luo, Q. Yu, Z. Liu, Q. Wang, W. Ren, C. Sun, H.-M. Cheng and B. Liu, *Nat. Commun.*, 2023, **14**, 3607.
27 Z. Li, Y. Yao, S. Sun, J. Liang, S. Hong, H. Zhang, C. Yang, X. Zhang, Z. Cai, J. Li, Y. Ren, Y. Luo, D. Zheng, X. He, Q. Liu, Y. Wang, F. Gong, X. Sun and B. Tang, *Angew. Chem. Int. Ed.*, 2024, **63**, e202316522.
28 H. Chen, P. Liu, W. Li, W. Xu, Y. Wen, S. Zhang, L. Yi, Y. Dai, X. Chen, S. Dai, Z. Tian, L. Chen and Z. Lu, *Adv. Mater.*, 2024, **36**, 2411302.
29 J. Wang, Y. Liu, G. Yang, Y. Jiao, Y. Dong, C. Tian, H. Yan and H. Fu, *Nat. Commun.*, 2025, **16**, 1319.
30 Q. Quan, Y. Zhang, H. Li, W. Wang, P. Xie, D. Chen, W. Wang, Y. Meng, D. Yin, Y. Li, D. Song, L. Chen, S. Li, C. Yang, T. Yanagida, C.-Y. Wong, S. Yip and J. C. Ho, *Nat. Commun.*, 2025, **16**, 2908.
31 J. Sun, S. Zhou, Z. Zhao, S. Qin, X. Meng, C.-H. Tung and L.-Z. Wu, *Energy Environ. Sci.*, 2025, **18**, 1952–1962.
32 H. Hu, X. Wang, Z. Zhang, J. Liu, X. Yan, X. Wang, J. Wang, J. P. Attfield and M. Yang, *Adv. Mater.*, 2025, **37**, 2415421.
33 J. Zhu, T. Cui, J. Chi, T. Wang, L. Guo, X. Liu, Z. Wu, J. Lai and L. Wang, *Angew. Chem. Int. Ed.*, 2025, **64**, e202414721.
34 Z. Li, M. Li, Y. Chen, X. Ye, M. Liu and L. Y. S. Lee, *Angew. Chem. Int. Ed.*, 2024, **63**, e202410396.
35 Z. Cai, J. Liang, Z. Li, T. Yan, C. Yang, S. Sun, M. Yue, X. Liu, T. Xie, Y. Wang, T. Li, Y. Luo, D. Zheng, Q. Liu, J. Zhao, X. Sun and B. Tang, *Nat. Commun.*, 2024, **15**, 6624.
36 L. Liao, D. Li, Y. Zhang, Y. Zhang, F. Yu, L. Yang, X. Wang, D. Tang and H. Zhou, *Adv. Mater.*, 2024, **36**, 2405852.
37 L.-W. Shen, Y. Wang, L. Shen, J.-B. Chen, Y. Liu, M.-X. Hu, W.-Y. Zhao, K.-Y. Xiong, S.-M. Wu, Y. Lu, J. Ying, M. M. Titirici, C. Janiak, G. Tian and X.-Y. Yang, *Energy Environ. Sci.*, 2024, **17**, 3888–3897.
38 X. Liu, Q. Yu, X. Qu, X. Wang, J. Chi and L. Wang, *Adv. Mater.*, 2024, **36**, 2307395.
39 J. Guo, Y. Zheng, Z. Hu, C. Zheng, J. Mao, K. Du, M. Jaroniec, S.-Z. Qiao and T. Ling, *Nat. Energy*, DOI:10.1038/s41560-023-01195-x.
40 T. Liu, C. Lan, M. Tang, M. Li, Y. Xu, H. Yang, Q. Deng, W. Jiang, Z. Zhao, Y. Wu and H. Xie, *Nat. Commun.*, 2024, **15**, 8874.
41 H. Shi, T. Wang, J. Liu, W. Chen, S. Li, J. Liang, S. Liu, X. Liu, Z. Cai, C. Wang, D. Su, Y. Huang, L. Elbaz and Q. Li, *Nat. Commun.*, 2023, **14**, 3934.
42 L. Zhou, D. Guo, L. Wu, Z. Guan, C. Zou, H. Jin, G. Fang, X. Chen and S. Wang, *Nat. Commun.*, 2024, **15**, 2481.
43 X. Sun, W. Shen, H. Liu, P. Xi, M. Jaroniec, Y. Zheng and S.-Z. Qiao, *Nat. Commun.*, 2024, **15**, 10351.

44 X. He, Y. Yao, L. Zhang, H. Wang, H. Tang, W. Jiang, Y. Ren, J. Nan, Y. Luo, T. Wu, F. Luo, B. Tang and X. Sun, *Nat. Commun.*, 2025, **16**, 4998.
45 X. Duan, Q. Sha, P. Li, T. Li, G. Yang, W. Liu, E. Yu, D. Zhou, J. Fang, W. Chen, Y. Chen, L. Zheng, J. Liao, Z. Wang, Y. Li, H. Yang, G. Zhang, Z. Zhuang, S.-F. Hung, C. Jing, J. Luo, L. Bai, J. Dong, H. Xiao, W. Liu, Y. Kuang, B. Liu and X. Sun, *Nat. Commun.*, 2024, **15**, 1973.
46 W. Liu, J. Yu, T. Li, S. Li, B. Ding, X. Guo, A. Cao, Q. Sha, D. Zhou, Y. Kuang and X. Sun, *Nat. Commun.*, 2024, **15**, 4712.